JGR Solid Earth

RESEARCH ARTICLE
10.1029/2023JB028362

GRACE and GRACE Follow-On Gravity Observations of Intermediate-Depth Earthquakes Contrasted With Those of Shallow Events

Shin-Chan Han[1], Jeanne Sauber[2], Taco Broerse[3], Fred Pollitz[4], Emile Okal[5], Taehwan Jeon[6], Ki-Weon Seo[7], and Richard Stanaway[8]

[1]School of Engineering, University of Newcastle, Callaghan, NSW, Australia, [2]Geodesy and Geophysics Laboratory, NASA Goddard Space Flight Center, Greenbelt, MD, USA, [3]Faculty of Civil Engineering and Geosciences, Delft University of Technology, Delft, The Netherlands, [4]U.S. Geological Survey, Menlo Park, CA, USA, [5]Department of Earth and Planetary Sciences, Northwestern University, Evanston, IL, USA, [6]Center for Educational Research, Seoul National University, Seoul, Korea, [7]Department of Earth Science Education, Seoul National University, Seoul, Korea, [8]Papua New Guinea University of Technology, Lae, Papua New Guinea

Key Points:

- Gravity changes after the intermediate-depth earthquakes are unexpectedly large and different from those of shallow events
- Stronger resistance of rocks to volume change at intermediate-depth results in highly incompressible deformation and gravity changes
- Two *Mw* 8.0 intermediate-depth earthquakes of 2016 & 2017 Papua New Guinea and 2019 Peru highlight compressibility in gravity change

Supporting Information:

Supporting Information may be found in the online version of this article.

Correspondence to:

S.-C. Han,
shin-chan.han@newcastle.edu.au

Citation:

Han, S.-C., Sauber, J., Broerse, T., Pollitz, F., Okal, E., Jeon, T., et al. (2024). GRACE and GRACE Follow-on gravity observations of intermediate-depth earthquakes contrasted with those of shallow events. *Journal of Geophysical Research: Solid Earth*, *129*, e2023JB028362. https://doi.org/10.1029/2023JB028362

Received 22 NOV 2023
Accepted 31 JAN 2024

Author Contributions:

Conceptualization: Shin-Chan Han, Jeanne Sauber
Data curation: Shin-Chan Han, Richard Stanaway
Formal analysis: Shin-Chan Han, Jeanne Sauber, Emile Okal
Funding acquisition: Shin-Chan Han
Investigation: Shin-Chan Han, Jeanne Sauber, Taco Broerse, Fred Pollitz, Emile Okal
Methodology: Shin-Chan Han, Jeanne Sauber, Taco Broerse, Fred Pollitz
Project administration: Shin-Chan Han, Jeanne Sauber

Abstract Earthquakes involve mass redistribution within the solid Earth and the ocean, and as a result, perturb the Earth's gravitational field. For most of the shallow (<60 km) earthquakes with $M_w > 8.0$, the GRACE satellite gravity measurements suggest considerable volumetric disturbance of rocks. At a spatial scale of hundreds of km, the effect of volumetric change exceeds gravity change by vertical deformation; for example, negative gravity anomalies associated with volumetric expansion are characteristic patterns after shallow thrust events. In this study, however, we report contrasting observations of gravity change from two intermediate-depth (100–150 km) earthquakes of 2016 & 2017 *Mw* 8.0 (two combined) Papua New Guinea thrust faulting events and 2019 *Mw* 8.0 Peru normal faulting and highlight the importance of compressibility in earthquake deformation. The combined 2016/17 thrust events resulted in a positive gravity anomaly of 5–6 microGal around the epicenter, while the 2019 normal faulting produced a negative gravity anomaly of 3–4 microGal. Our modeling found that these gravity changes are manifestation of vertical deformation with limited volumetric change, distinct from gravity changes after the shallow earthquakes. The stronger resistance of rocks to volume change at intermediate-depth results in largely incompressible deformation and thus in a gravity change dominated by vertical deformation. In addition, malleable rocks under high pressure and temperature at depth facilitated substantial afterslip and/or fast viscoelastic relaxation causing additional vertical deformation and gravity change equivalent to the coseismic change. For the Papua New Guinea events, this means that postseismic relaxation enhanced coseismic uplift and relative sea level decrease.

Plain Language Summary For the last two decades, changes in the global gravity field have been measured by the US-German Gravity Recovery And Climate Experiment (GRACE) and GRACE Follow-On satellites. The data quantify surface mass redistribution associated with water and ice mass changes as well as solid Earth mass changes such as earthquake deformation. From the GRACE data at a scale of several hundreds of km, we inferred that gravity changes after shallow (<60 km) earthquakes involve significant volumetric changes within the crust as well as vertical deformation. By contrast, in this study, we report gravity changes following two thrust faulting intermediate-depth (100–150 km) earthquakes in Eastern Papua New Guinea in 2016 and 2017, combining to M_w 8.0, and a normal faulting one in 2019 Peru (M_w 8.0), which differ significantly from the signals following shallow events. Our numerical modeling of coseismic and postseismic processes suggests that the deformation associated with these intermediate-depth earthquakes was largely incompressible due to higher resistance of rocks to volume change. Gravity changes observed by the satellites was due to vertical deformation, with little effect from volume change. This study demonstrates the contrasting examples of gravity changes depending on depth of ruptures (compressibility of rocks) and reiterates the importance of volume change in large-scale gravity changes.

1. Introduction

Great earthquakes ($M_w \geq 8.0$) are known to occur predominantly within the shallow layers of subduction zones (depth ≤70 km) and most of those, during the GRACE−GRACE-Follow-On era (2002-present), ruptured as thrust events when the cumulative stress building up at the interface between colliding plates exceeded the friction

Resources: Shin-Chan Han, Jeanne Sauber
Software: Shin-Chan Han, Taco Broerse, Fred Pollitz
Supervision: Shin-Chan Han
Validation: Shin-Chan Han, Jeanne Sauber, Taco Broerse, Fred Pollitz, Emile Okal, Taehwan Jeon, Ki-Weon Seo, Richard Stanaway
Visualization: Shin-Chan Han
Writing – original draft: Shin-Chan Han, Jeanne Sauber
Writing – review & editing: Shin-Chan Han, Jeanne Sauber, Taco Broerse, Fred Pollitz, Emile Okal, Taehwan Jeon, Ki-Weon Seo, Richard Stanaway

threshold (see Figure 1 of Lay (2015)). Much less frequently, strike-slip earthquakes within the oceanic plate (e.g., Wharton Basin, Indian Ocean, 2012, M_w = 8.6) as well as normal faulting events (e.g., Kuril Islands, 2007, M_w = 8.1; nucleation phase of Samoa, 2009, M_w = 8.0) were also recorded at comparable moment magnitudes (e.g., Beavan et al., 2010; Delescluse et al., 2012; Han et al., 2016). Finally, the deepest parts of subducting slabs can host truly great, if rare, earthquakes (e.g., Sea of Okhotsk, 2013, M_w = 8.3; Fiji, 2018, M_w = 8.1).

On 17 December 2016 and 22 January 2017, two M_w 7.9 (or M_w 8.0, combined) earthquakes occurred at intermediate depths east of New Ireland, Papua New Guinea. Estimates of their depths and focal mechanisms from seismic data indicate they happened within the subducting slab of the Solomon microplate below the Pacific plate; the 2016 event also included a triggered shallow rupture at the interface of the two colliding plates (USGS, https://earthquake.usgs.gov/earthquakes/eventpage/us200081v8/executive; See also supporting Figure S1 in Supporting Information S1). The 2016 event had a significant shallow slip portion (60% of the moment release) and it lasted ~80 s. In contrast, the 2017 event was quite deep (centroid moment was at a depth of ~150 km) and with a very compact, high-slip, fast source time function (<20 s) (from USGS finite fault slip plots; See supporting Figure S2 in Supporting Information S1). Another contrast was that the 2016 event had a very large number of shallow aftershocks ($M_w \geq 4.0$) within the first month with scattered aftershocks down to intermediate depths; whereas the 2017 event had fewer aftershocks and they were generally deeper except for scattered background seismicity typical of this area.

On 26 May 2019, a normal faulting earthquake of similar size (M_w 8.0) and similar source depth (~110 km) occurred in northern Peru within the subducting slab of the Nazca plate (USGS, https://earthquake.usgs.gov/earthquakes/eventpage/us60003sc0/executive) as it bends to dive more steeply beneath the South American plate. As is generally typical of intermediate depth earthquakes, this event had very few aftershocks ($M_w \geq 4.0$) (Liu & Yao, 2020; Vallée et al., 2023; Ye et al., 2020).

In this study, we report that both the combined effect of the 2016/2017 earthquakes and the 2019 Peruvian intermediate-depth event were detected in the satellite gravity data of the Gravity Recovery And Climate Experiment (GRACE) and its Follow-On (GRACE-FO); hereafter, we use GRACE to refer to both data sets. In this study, we do not differentiate the 2016 and 2017 events that occurred within a time difference of approximately one month and focus on their combined effect on the monthly gravity change. Detection of such gravity changes is rather unexpected since the seismic moment estimates of these events are generally thought to be at or below the resolution threshold of the GRACE data.

A number of gravity change studies following large shallow earthquakes have discussed two dominant effects causing perturbations in gravity, namely large-scale crustal density changes and vertical uplift or subsidence at density interfaces within the solid Earth and its surface (e.g., Okubo, 1992 for a half space modeling; Sun & Okubo, 1993; Pollitz, 1997a for a spherical Earth modeling). Those studies identified crustal deformation associated with volumetric change over an extensive region from the satellite observations (e.g., Han et al., 2006; Heki & Matsuo, 2010; Ogawa & Heki, 2007; Panet et al., 2007). They concluded that the total changes in surface gravity at large spatial scales (as detectable by satellites) are dominated by volumetric dilatation, as observed repeatedly for shallow thrust and strike-slip events (e.g., Han et al., 2013). In oceanic regions, this long wavelength gravity change is amplified by the relative sea level response to large-scale vertical motion (Broerse et al., 2011; Cambiotti et al., 2011; de Linage et al., 2009; Han et al., 2006). The observed gravity changes induced by shallow thrust events (e.g., Chao & Liau, 2019 and references therein) are markedly different from those due to the great deep earthquakes (depth ≥600 km) of 2013 Sea of Okhotsk and 2018 Fiji, for which the effect of a density change was greatly reduced in large-scale gravity observations (Tanaka, 2023; Tanaka et al., 2015; Xu et al., 2017).

According to a global average Earth model such as Preliminary Reference Earth Model (PREM) (Dziewonski & Anderson, 1981), the bulk modulus of crustal rocks varies from 50 to 75 GPa, values small enough to permit dilatation or contraction of rocks and perturb gravity over an extensive region, at a level detectable by GRACE satellites for events with Mw > 8.0. Figures 1 through 4 of Han et al. (2013) demonstrate how the elastic gravity perturbation changes with the depth of dislocation source. They illustrate that, for a given seismic source, depending on the magnitude of the bulk modulus at source depth, the gravity anomaly is largely governed by the material compressibility, and can even change in sign (see the monopole component of gravity change in Figure 4 of Han et al. (2013)). The gravity observations after the 2016/2017 and 2019 intermediate-depth earthquakes are an opportunity to elucidate how differently the solid Earth deforms after earthquakes in association with different material compressibility at depth, in contrast to the response seen following shallow events.

The failure mechanism of intermediate-depth earthquakes is believed to be different from the stick-and-slip framework of shallow events (Savage, 1983), due to the high temperature and pressure environment which makes the ambient rocks ductile and behaving differently from shallow crustal rocks (e.g., Kelemen & Hirth, 2007). In this study, we present detailed data analyses of the GRACE gravity observations in conjunction with modeling of elastic deformation and viscoelastic relaxation, in order to understand characteristics of deformation possibly different from those of shallow earthquakes.

The 2016/2017 earthquakes occurred near South Pacific islands that are impacted by absolute sea level rise due to climate change (e.g., Becker et al., 2012). Earthquake-induced vertical land motion and geoid height changes both contribute to relative sea level changes, the apparent sea level changes as experienced at the coast (e.g., Broerse et al., 2011). In similar settings of islands along subduction zones, tectonic vertical land motion is dominant over other contributions to relative sea level change (e.g., Ballu et al., 2011). We study how the earthquake-induced deformation affects local vertical land motion and relative sea level change, based on numerical modeling and measurements of vertical land motion from campaign GPS surveys.

2. Gravity Changes After the Intermediate-Depth Earthquakes of 2016/2017 and 2019

We have processed two decades of monthly global gravitational potential data sets from GRACE (2002–2017) and GRACE-FO (2018–2023), provided in the form of a set of Stokes coefficients, and known as Level-2 (L2) data products, from the University of Texas Center for Space Research. As suggested by the NASA project (stated in Technical Notes 11 and 14), the first two zonal coefficients of C_{20} and C_{30} were replaced with those of the Satellite Laser Ranging (SLR) solutions (Cheng & Ries, 2023; Loomis et al., 2020). Some better-known geophysical mass variations including solid Earth and ocean tidal variations, pole tides, and non-tidal oceanic and atmospheric mass changes have been modeled a priori so that the resulting L2 data present un-modeled and mis-modeled geopotential variations (Yuan, 2019). These are primarily associated with surface mass variations due to the water cycle and to polar region ice melting (e.g., Tapley et al., 2019), and with solid Earth mass changes in the form of earthquake deformation (coseismic and postseismic), as well as with glacial isostatic adjustment (e.g., Tamisiea et al., 2007).

Due to satellite instrument noise (primarily from the intersatellite ranging system and accelerometers), satellite orbital altitude (∼480 km above the sea level), and mis-modeled high frequency mass variability (aka temporal aliasing), the monthly mean estimates like the L2 coefficients suffer from increasing noise with increasing degree of the spherical harmonic function. On a global average, spherical harmonics with degree and order up to 40–50 (equivalently 400–500 km in spatial resolution) would correspond to the maximum resolution of the monthly L2 data. Although several post-processing filtering and application-specific algorithms have been examined by the community (e.g., Wahr et al. (1998) and numerous variants), we intentionally apply the simplest data processing in this section, to highlight that the signals are clear even without sophisticated processing. (Later, we will examine a method tailored to earthquake signal detection.) We use a truncation at the spherical harmonic degree of 60 with a cosine tapering starting from degree 30 to reduce the ringing effect of spectral truncation (i.e., Gibbs' phenomenon); the effective resolution is degree 45 (or ∼450 km).

Using the postprocessed monthly L2 geopotential coefficients, we calculated the time series of gravity change maps from April 2002 to May 2023, which are nearly continuous, except for a major gap (July 2017–May 2018) between the GRACE and GRACE-FO satellite missions. The gravity change is computed as the radial derivative of geopotential change and evaluated at the mean spherical Earth's surface on which the L2 geopotential coefficients are defined (Yuan, 2019). The use of the ellipsoidal reference surface (e.g., Ditmar, 2018) is not important for the spatial resolution and latitude range of this study.

We determined the gravity change by earthquakes by estimating a Heaviside step out of the monthly gravity data. Figure 1a presents the estimated gravity change map at the epoch 2017.01 that is the average decimal year of the two M_w 7.9 intermediate-depth events that occurred on 17 December 2016 and 22 January 2017. The epicenters are separated by only ∼250 km (see the focal mechanism diagrams in Figure 1). The gravity change of up to 5–6 microGal are clearly detectable around the epicentral region. The spatial size of the anomaly within the detectable range is about 600 km. The monthly time series of gravity change at the center of the gravity anomaly (6°S, 155°E) is shown in Figure 1b; it does not present any evident seasonal pattern nor any interannual trend of a background change (like ocean mass). We estimated the coseismic gravity change at 2017.01 to be 5.5 ± 0.3 microGal. The postseismic gravity change seems to be small or very fast only during the first few months, which is substantially

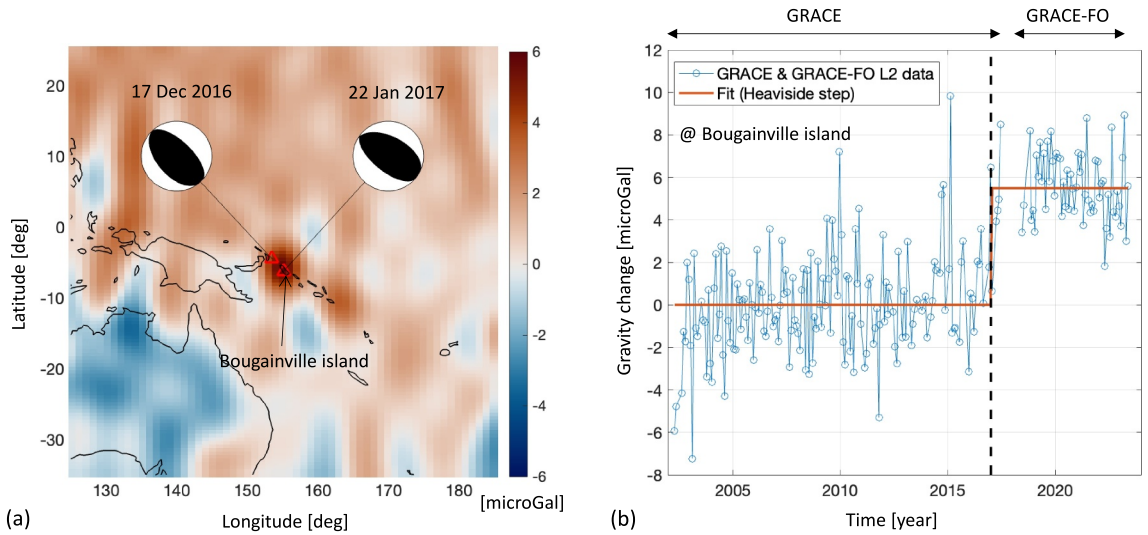

Figure 1. (a) Gravity change after the 2016/17 earthquakes estimated from monthly GRACE and GRACE-FO global gravitational potential fields. The offset was computed by estimating the Heaviside step change from the entire data sets. The red triangles show the epicenters of the events. (b) The time series of the observed gravity changes at the location (6°S, 155°E) of Bougainville Island. The red line is the best fit to the earthquake-related offset in the data, estimated at 5.5 ± 0.3 microGal. The vertical dashed line shows the average epoch of the two events in 2016 and 2017.

different from the long-lasting gravity changes observed after shallow events of a similar or greater magnitude (e.g., Han et al., 2014).

Figure 2 shows the gravity change induced by the 26 May 2019 *Mw* 8.0 normal faulting event in Peru. Figure 2a presents the gravity change map estimated by fitting the Heaviside step change at 2019.4. In the northern part of Peru (the western part of the Amazon river basin), a negative gravity change of 3–4 microGal was found around the epicenter. The magnitude of the coseismic change is smaller than the combined 2016/2017 thrust events while the spatial size of the anomaly is similar. Other signals also present likely originated from interannual variation of seasonal hydrological water mass changes. The epicenter is next to the Amazon River basin, which features the largest seasonal gravity variation due to its hydrological cycle. The gravity time series at the epicenter (5°S, 285° E) indeed show a significant seasonal change of 12 microGal (peak-to-peak) with interannual variation

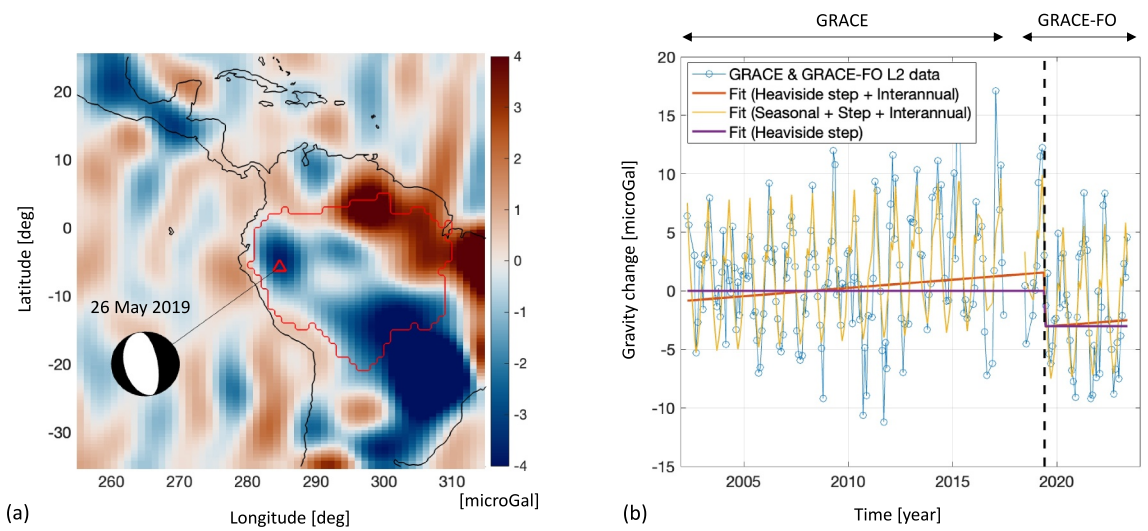

Figure 2. The same as Figure 1 but for the 2019 Peru earthquake. This area covers the Amazon river basin whose boundary is shown in red. The earthquake occurred in the western part of the river basin. At the center of the negative gravity anomaly near the epicenter, the earthquake-related gravity change at the location of (5°S, 285°E) is estimated to be −4.6 ± 0.8 microGal without inclusion of a linear trend and −3.0 ± 0.6 microGal with a linear trend. The observed gravity changes also include the seasonal change (12 microGal peak-to-peak) by hydrological mass loading with interannual variation.

(Figure 2b). The seasonal pattern, a linear trend for interannual hydrological variation, and a Heaviside step attributable to the earthquake, were simultaneously estimated from the monthly gravity data. The seasonal patterns were estimated by 12 parameters representing 12 monthly means of the entire time series. The coseismic change was estimated to be -4.6 ± 0.8 microGal without a linear trend and -3.0 ± 0.6 microGal with a linear trend. (In both cases, the Student's t-values of the Heaviside step estimates are 5–6, while the critical *t*-value at the 95% confidence level with a degree of freedom of ~200 is 1.97. Therefore, the Heaviside step parameter is significantly different from zero at the 95% confidence level). Although the coseismic change is, to some extent, obscured by large seasonal and interannual changes in hydrological loads, there is a statistically significant gravity decrease after the earthquake. It is also seen that the baseline of the seasonal change lowered after the event as seen from the last four consecutive cycles of the seasonal gravity change observations. Such gravity measurements would complicate a hydrological study in Peru unless the earthquake-induced change is addressed, like the case of the 2010 Maule, Chile earthquake interfering with the drought signal estimates in southern Argentina (Rodell et al., 2014).

These 2016/17 thrust and 2019 normal faulting events are the first intermediate-depth earthquakes detected using satellite gravity measurements, and they feature opposite-type focal mechanisms. We examine these gravity change observations by considering coseismic (elastic) deformation in a compressible Earth model with radially stratified density layers like PREM, and viscoelastic relaxation.

3. Deformation and Gravity Changes by Shallow Versus Intermediate-Depth Earthquakes

The observed spatial patterns of gravity changes of the 2016/2017 thrust earthquakes contrast with those of shallow inter-plate subduction zone events, including the great earthquakes in 2004, 2007, 2010, 2011 (Han et al., 2013). Shallow thrust events involve substantial deformation by volumetric expansion, resulting in a drop in ambient rock density in the region of major slip (e.g., Okubo (1992) and see also Materials and Methods of Han et al. (2006)). The bulk modulus (i.e., resistance to compression) of the rocks at depths typical of shallow events is relatively small (50–75 GPa), allowing extensive dilatation over a wide region, thus leading to a broad negative gravity change, which is strong at the typical wavelengths that are resolvable with GRACE data. This volumetric effect is compensated, in the total gravity change, by the effect of vertical deformation. For shallow thrusting, uplift occurs above the updip limit of slip and subsidence above the downdip limit, resulting in positive and negative gravity changes in regions of uplift and subsidence, respectively. For shallow thrust events, with contributions of dilatation and vertical deformation combined, it is typical to observe a coseismic positive gravity change by localized uplift of the hanging wall and a negative gravity change due to extensive dilatation and subsidence above the deep parts of the rupture. This characteristic spatial pattern of gravity changes has consistently been observed in satellite measurements, following shallow thrust events (e.g., Han et al., 2013). However, the volumetric effect is difficult to measure from ground-borne instrumentation, which is more sensitive to local (and thus vertical) deformation. By contrast, according to the globally averaged PREM model, the bulk modulus corresponding to layers surrounding intermediate-depth earthquakes is two or three times larger (130–150 GPa) than that of shallow events. Thus, the surrounding rocks are more resistant to volumetric change. How does that affect the resulting deformation and gravity change?

In order to quantitatively understand deformation under small and large bulk moduli, we computed synthetic gravity changes from imposed finite fault dislocations at mean depths of 15 and 100 km (Figure 3). The seismic moment was held fixed at 1.33×10^{20} N-m. We set the dip angle to 50°, the rake angle to 90° (simulating thrust slip), the fault strike to 0°E (dipping east), and the fault length and width to 50 and 20 km, respectively. The center of the lower edge of the fault plane is located at latitude 0° and longitude 0°. We computed the surface vertical deformation and the gravity change above the center of the fault plane, in a model where the top layer represents the ocean. The ocean layer contributes to gravity change through its density contrast from the upper crustal layer, while the contributions from absolute sea level changes is much smaller (e.g., Broerse et al., 2011; Han et al., 2006). In addition to the surface vertical motion, we also examined the vertical deformation at the interfaces of the upper and lower crust and of the lower crust and upper mantle, as these two additional major density discontinuities can affect surface gravity changes (e.g., Han et al., 2006). We used the computer code STATIC1D for computation of coseismic deformation, strain and gravity changes from a dislocation slip in a spherically layered elastic Earth model consistent with PREM (Pollitz, 1996, 1997b).

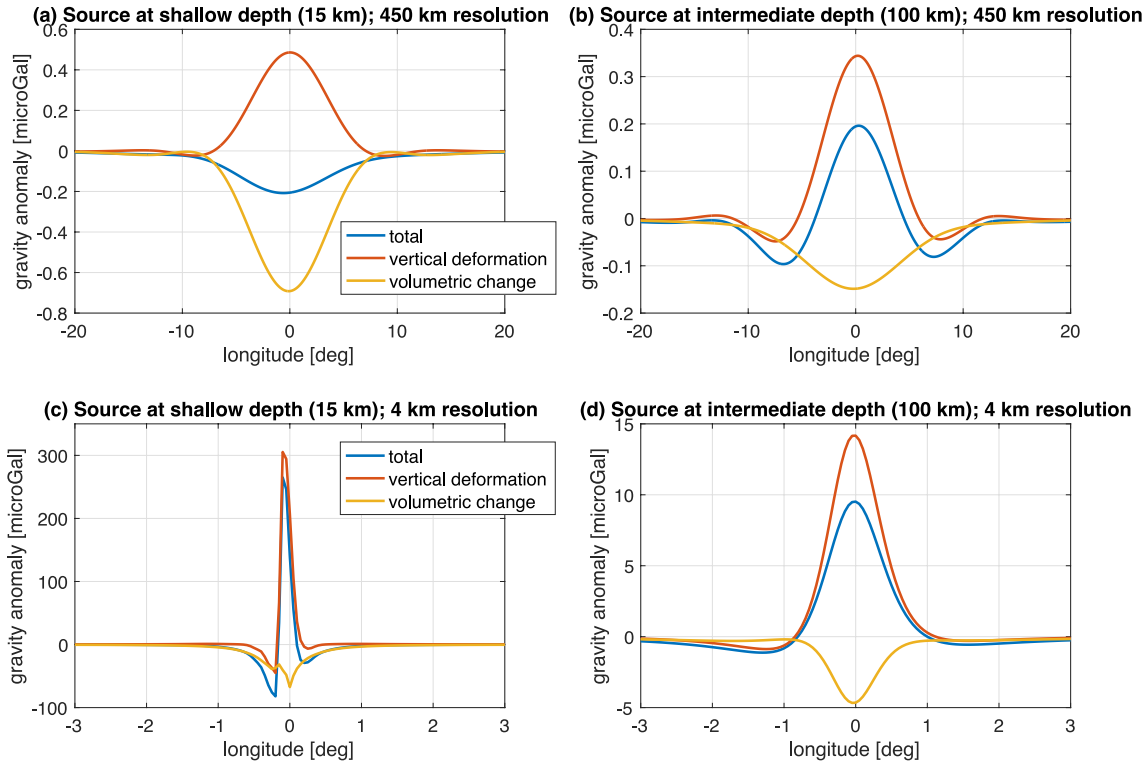

Figure 3. (a) The elastic gravity changes by a synthetic thrust-faulting source at 15 km depth; the total gravity change (blue) is a composite of the gravity changes by vertical deformation at the density interfaces between the ocean, upper crust, and lower crustal layers (red) and by volumetric change (yellow). (b) The same as (a) from a source with the same moment magnitude, but at 100 km depth. (a) and (b) show the model gravity change at the resolution of 450 km while (c) and (d) present the same but at the resolution of 4 km.

Figure 3a presents the computed surface gravity change by a shallow source at 15 km depth with the results shown for a spatial resolution of 450 km, approximately commensurate with the GRACE data. We separate volumetric and vertical deformation related gravity changes by removing the effect of vertical deformation at density interfaces from the total gravity change (see the supporting online material of Han et al. (2006)). The total gravity change is negative, as large as −0.2 microGal. This is the result from two opposite contributions: (a) the gravity change by vertical deformation primarily of the top three density interfaces, which produces a positive gravity change of 0.5 microGal; and (b) the gravity change by volumetric expansion (computed by total gravity change minus the result from (a)), which peaks around −0.7 microGal. At this spatial scale, the volumetric gravity change is greater than the effect of vertical deformation, resulting in a negative final gravity anomaly. The competing effect of volumetric expansion and vertical deformation to gravity change is found to be more extreme with a lower dip angle, which is more representative of shallow thrust events.

In contrast, for the same source located at 100 km depth (Figure 3b), the surface gravity change has a positive value of 0.2 microGal. The gravity change by vertical deformation is 0.35 microGal, and the gravity change by volumetric expansion is only −0.15 microGal. Consequently, the total surface gravity change of 0.2 microGal is dominated by the vertical deformation. This is the opposite of the case of a shallow event, and essentially results from the reduced compressibility of the ambient rocks at a greater depth. The effect of bulk modulus change with depth is so drastic that it can even change the sign of the surface gravity anomaly on a spatial scale of several hundreds of km. This simple model explains the positive gravity observation from GRACE after the 2016/2017 thrust events, which is markedly different from the predominantly negative anomalies that have been observed after shallow thrust earthquakes.

Figures 3c and 3d illustrate the same cases but for the full spatial resolution (suitable for ground geodetic measurements like GPS and InSAR). The overall size of gravity changes is amplified with increased spatial resolution, and, in both cases, the vertical deformation is the dominant effect on surface gravity change. The

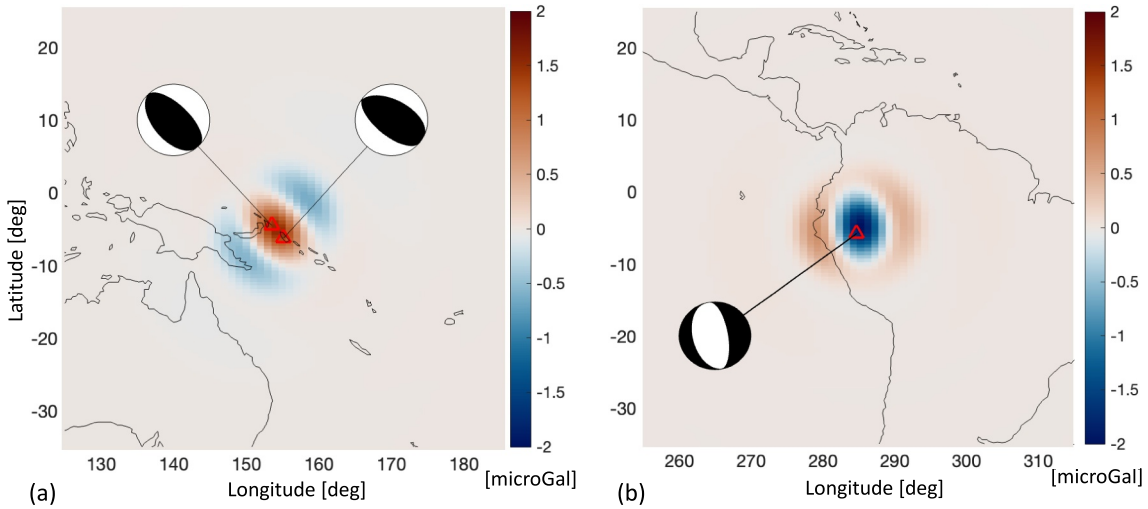

Figure 4. (a) The predicted elastic gravity changes by the 2016/17 thrust earthquakes, presented at the same resolution (450 km) as the GRACE & GRACE-FO observations in Figure 1. (b) The synthetic gravity changes from the 2019 normal faulting earthquake. The seismic source models of the centroid moment tensor from USGS were used. The red triangles show the epicenters of the events. Note: these predicted gravity anomalies are considerably smaller than the observed gravity change offset.

smooth nature of the gravity change in Figure 3d is due to the fall-off of the gravitational potential over a greater distance from the deeper source and smoothing of deformation due to the thicker overlying layer.

4. Elastic and Viscoelastic Relaxation Models

We examined the gravity changes using the finite fault models of two distinct events (combined thrust in 2016/2017 and normal faulting in 2019) available from the USGS website. The combined seismic moment for the 2016/2017 thrust ruptures (with largely constructive interference) is 18×10^{20} N-m and that of the 2019 normal faulting is 12×10^{20} N-m. The depth estimates of various centroid moment tensor solutions range widely from 95 to 135 km, with a few tens of km uncertainty. Based on the available finite fault solutions and the PREM model, and using the STATIC1D code, we computed surface gravity changes. Since STATIC1D is based on a spherical harmonic synthesis of normal modes, the exact same truncation and tapering used in the GRACE data processing were applied for a consistent comparison.

Figure 4 presents the computed surface coseismic gravity changes for the two different regions. Note that the gravity computations include a model ocean layer for the 2016/2017 events but no ocean layer for the 2019 event, reflecting their respective geographic environments. The synthesis yields elastic deformation and gravity changes of as much as 2 microGal for the 2016/2017 thrust, and −2 microGal for the 2019 normal faulting event, over a wide area of a few hundred km. When compared to the GRACE observations (Figures 1 and 2), the models are consistent with the observed spatial patterns but significantly underestimate the size of gravity changes, by a factor of 2–3 (depending on how we interpret the measurements of gravity changes with or without a linear trend of background mass change). Such a large mismatch in the amplitude is too large to be attributed to the uncertainty of the seismic model estimates for these events. For shallow earthquakes, substantial aseismic slip and/or viscoelastic deformation follow the ruptures. We now consider how the postseismic response to these intermediate-depth earthquakes may be different from the viscoelastic relaxation triggered by shallow sources.

We have developed a technique to decompose the monthly L2 geopotential data into five independent and mutually orthogonal gravity changes associated with the five independent moment tensor components of a double-couple point source (e.g., Han et al., 2014). This method effectively eliminates non-earthquake signals from global geopotential observations and makes the model comparison tractable particularly when a model of viscoelastic relaxation is computed based on the spherical harmonic normal modes (e.g., Broerse et al., 2015; Pollitz, 1992). For a double-couple point source, the excited gravity change $\gamma(\theta,\varphi,t)$ at latitude θ, longitude φ, and time t can be expressed as follows:

$$\gamma(\theta,\varphi,t) = \left(\frac{-M_{rr}}{2}\right) g_{rr}(\theta,\varphi,t) + M_{r\theta}\, g_{r\theta}(\theta,\varphi,t) + M_{r\varphi}\, g_{r\varphi}(\theta,\varphi,t)$$
$$+ \left(\frac{M_{\theta\theta} - M_{\varphi\varphi}}{2}\right) g_{\theta\theta-\varphi\varphi}(\theta,\varphi,t) + M_{\theta\varphi}\, g_{\theta\varphi}(\theta,\varphi,t), \quad (1)$$

where the five moment tensor components of the source are M_{rr}, $M_{r\theta}$, $M_{r\varphi}$, ($M_{\theta\theta}$−$M_{\varphi\varphi}$), and $M_{\theta\varphi}$, and they are multiplied with the corresponding elastic and viscoelastic response functions (Green's functions) $g_{rr}(\theta,\varphi,t)$, $g_{r\theta}(\theta,\varphi,t)$, $g_{r\varphi}(\theta,\varphi,t)$, $g_{\theta\theta-\varphi\varphi}(\theta,\varphi,t)$, and $g_{\theta\varphi}(\theta,\varphi,t)$. The five response functions in the right-hand side of Equation 1 are mutually orthogonal and this property is very useful to decompose the observed GRACE geopotential data into those five components of gravity changes (see Figure 2 of Han et al. (2014) and Figure 3 of Han et al. (2015)).

Then, we define the viscoelastic time-history functions for each of the components as spatial integrals of the viscoelastic and the static Green's functions. For example, in the case of the monopole component (M_{rr}), the time-history function is written as

$$\eta_0(t) = \int g_{rr}(\theta,\varphi,t)\, e_{rr}(\theta,\varphi)\, d\Omega \Big/ \int e_{rr}(\theta,\varphi)^2 d\Omega, \quad (2a)$$

where $e_{rr}(\theta,\varphi)$ is the (time-independent) static Green's function and the integrals are taken over the Earth's surface (Ω). For other components (dipole and quadrupole), similar time-history functions can be computed as follows:

$$\eta_1(t) = \int g_{r\theta}(\theta,\varphi,t)\, e_{r\theta}(\theta,\varphi)\, d\Omega \Big/ \int e_{r\theta}(\theta,\varphi)^2 d\Omega, \quad (2b)$$

$$\eta_2(t) = \int g_{\theta\varphi}(\theta,\varphi,t)\, e_{\theta\varphi}(\theta,\varphi)\, d\Omega \Big/ \int e_{\theta\varphi}(\theta,\varphi)^2 d\Omega. \quad (2c)$$

Note that the time-history functions corresponding to $M_{r\varphi}$ and $M_{\theta\theta}$−$M_{\varphi\varphi}$ are the same as Equations 2b and 2c, respectively. Therefore, there are only three independent time-history functions in any viscoelastic relation model accounting for a 1D-layered Earth model, in analogy to the existence of only three independent excitation coefficients for an elastic Earth (K_0, K_1, and K_2 in the notation of Kanamori and Cipar (1974)). These functions essentially describe how the surface gravity anomaly changes viscoelastically over time, relative to the elastic change (e.g., supporting information of Han et al. (2014)).

Figure 5 shows two sets of examples of the time-history functions: top-panels for a synthetic point source at 15 km depth and bottom-panels for one at 100 km. As indicated, there are three functions (monopole, dipole and quadrupole components) for each set and each panel shows the elastic-only (i.e., a Heaviside step function) and four cases of the Burgers viscoelastic models including a Maxwell viscosity of 10^{19}, 4×10^{19}, 7×10^{19}, and 10^{20} Pa s with a fixed Kelvin viscosity of 10^{18} Pa s and the Kelvin shear modulus constrained to the elastic shear modulus for the asthenosphere (60–220 km). All other Earth model parameters are consistent with the PREM elastic structure and include the assigned upper and lower mantle viscosities of 5×10^{20} and 10^{22} Pa s, respectively. The model also includes an ocean layer.

For the shallow source (15 km) within a layer with a low incompressibility (bulk modulus) of 52 GPa, the viscoelastic gravity change of the monopole component is in a direction opposite to the elastic change. The relative magnitude of the time-dependent change is largest for the monopole component, followed by the quadrupole component; but the quadrupole change is in the same direction as the elastic change. The dipole pattern has the smallest viscoelastic gravity change, while being opposite to the elastic change. In contrast, for the intermediate-depth (100 km) source within a layer with large resistance to compression (a bulk modulus of 130 GPa), all gravity changes are additive to those of the elastic change, and due mostly to vertical deformation with considerably smaller volume change in comparison to shallow earthquakes. As in the case of shallow sources, most of the time-dependent changes with respect to the elastic gravity changes result from the monopole and quadrupole patterns. This leads to the conclusion that, for any earthquake featuring a dominant dipole moment, its viscoelastic gravity change will be smaller than the viscoelastic gravity change by earthquakes with

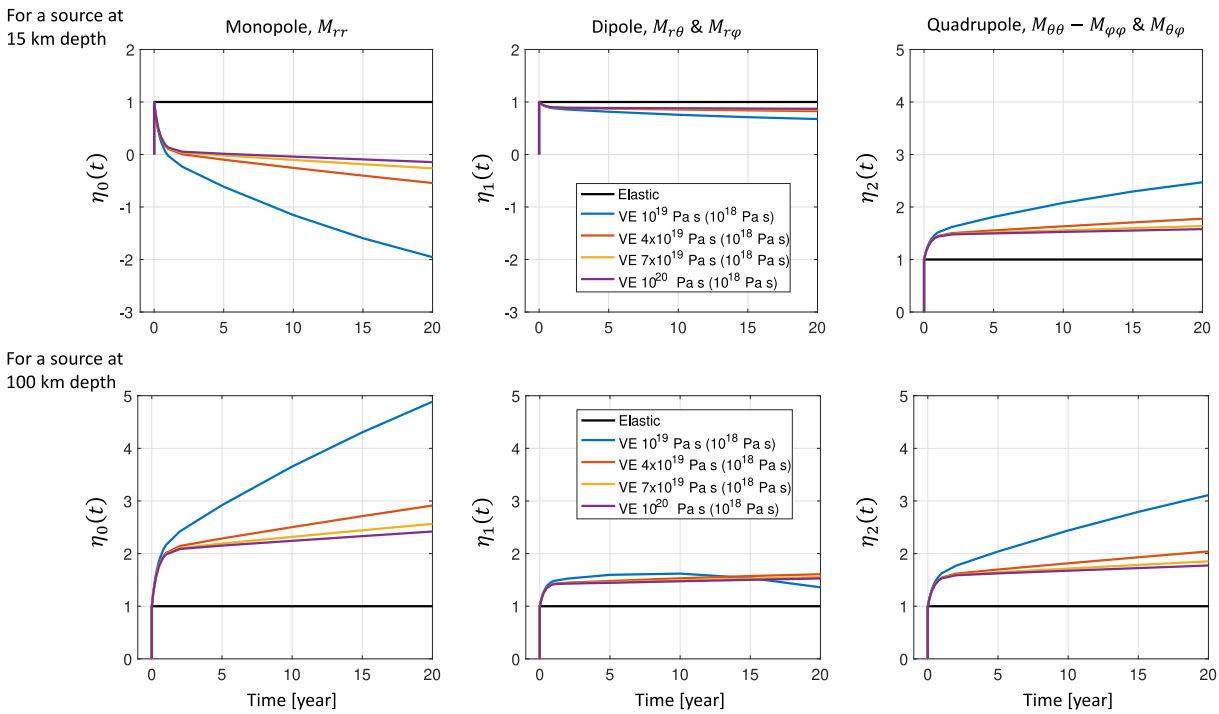

Figure 5. Various synthetic gravity changes as a function of time and asthenosphere viscosity. The model gravity changes include the elastic (E) model in black and viscoelastic (VE) models in various colors as denoted in the legend. For VE models, the transient viscosity of the asthenosphere was fixed at 10^{18} Pa s and various steady-state viscosities ranging from 10^{19} to 10^{20} Pa s were examined. The gravity change was normalized with the elastic gravity change and the earthquake was assumed to occur at year zero. Top panels show the gravity changes from a source at 15 km depth, while the bottom panels are computed with a source at 100 km depth. Three distinct gravity changes corresponding to the monopole, dipole and quadrupole patterns were examined in each case. Note that the total gravity change is nothing but a combination of these three components of changes scaled with the five moment tensor components. This model test highlights how the source depth and viscosity produce different gravity changes over time.

the same seismic moment but with dominantly monopole and/or quadrupole components. This may be explained since a viscous layer such as the asthenosphere yields more effectively to a horizontal shear (monopole and quadrupole) than to a vertical shear (dipole). In other words, the dislocation of the dipole source puts the coseismic stress change in a less effective radial direction for viscoelastic relaxation.

The two examples of Figure 5 also highlight the source depth and thus the incompressibility of the ambient rocks as a governing factor of viscoelastic gravity changes, particularly for the monopole pattern. The additive nature of the elastic and viscoelastic gravity changes from intermediate-depth earthquakes leads, over a period of 5 years after the event, to a gravity anomaly amplified two or more times with respect to the elastic gravity change, depending on the effective viscosity at depth. Thus, gravity changes by earthquakes from intermediate-depth sources would be more detectable by satellite gravimetry than the ones from shallow sources of the same magnitude.

5. Postseismic Gravity Change Observations

After applying the decomposition method (see supporting information of Han et al. (2014)), as in Equation 1, to the entire GRACE and GRACE-FO measurements of global gravity fields, we obtained the time series of gravity changes for each of the components of the right-hand side of Equation 1, shown in Figures 6 and 7, respectively, for the 2016/2017 and 2019 events. The GRACE gravity time series were effectively scaled by the elastic gravity change so that the resulting time series were represented in terms of seismic moment change over time in 10^{20} N-m. If there were no viscoelastic change, no aseismic slip, no data noise, and no other non-earthquake signal, the time series would feature only a Heaviside step with the magnitude of the step corresponding to each component of the released seismic moment. With actual observations, measurement noise and other remaining non-earthquake signals will appear, in addition to earthquake deformation signals.

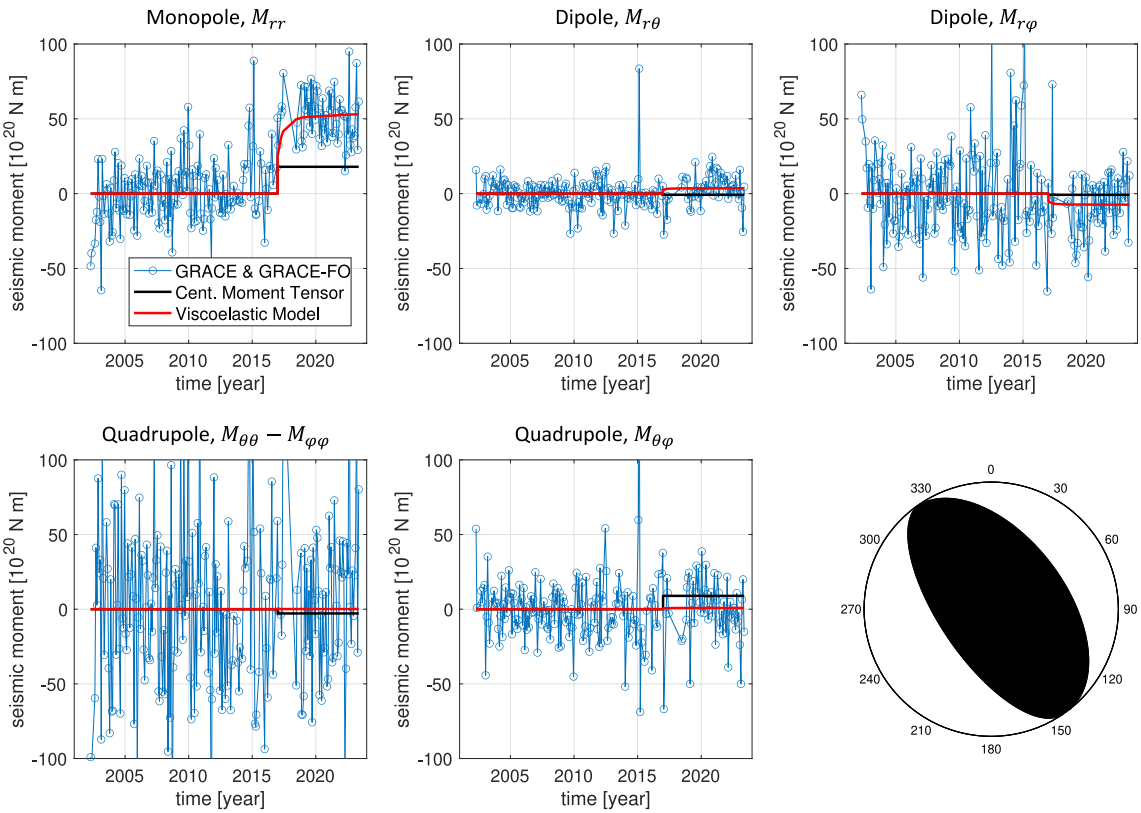

Figure 6. The GRACE and GRACE-FO observations of gravity changes corresponding to five moment tensor components for the 2016/17 earthquakes (blue circles). The elastic (black) and viscoelastic (red) models were compared with the observations. The composite of USGS centroid moment tensor solutions of the 2016 and 2017 events were used for the seismic source models. Depicted is the viscoelastic model with a transient viscosity of 10^{18} Pa s and a steady-state viscosity of 5×10^{19} Pa s. The focal mechanism diagram was determined from the GRACE gravity observations.

Figure 6 shows two decades of gravity change observations, after being decomposed into the five moment tensor components at the average location of the 2016 and 2017 events (i.e., the moment weighted average epicenter) from GRACE and GRACE-FO monthly L2 data, and the synthetic gravity changes from the elastic and viscoelastic deformation models (like Figure 5). Note that each of the time series exhibits different amplitudes of noise in the data. Among the five, the $M_{r\varphi}$ and ($M_{\theta\theta}$−$M_{\varphi\varphi}$) are the least accurate due to the orbital sampling nature of the GRACE satellites, which makes them more sensitive to changes in N-S direction than in E-W direction. According to the seismic moment tensor solutions of the 2016/2017 combined event, the largest moment release was found from the monopole M_{rr} component with an amplitude of $\sim 18 \times 10^{20}$ N-m (black lines), followed by the quadrupole component of $M_{\theta\varphi}$, but less significant compared to the gravity data noise. The observation of M_{rr} time series shows a change 2–3 times larger than the seismic solutions. Moreover, while the 2011 Tohoku-Oki shallow thrust event showed postseismic changes over the first two years as large as, and in the opposite direction to, the coseismic change (see Figure 2 of Han et al. (2014)), the 2016/2017 intermediate-depth events feature an M_{rr} change in the same direction as the coseismic change. Once again, this is due to the opposite coseismic gravity changes from shallow *vs*. intermediate-depth thrusts under contrasting incompressibility.

We tested various cases of bi-viscous rheology and viscosity in the asthenosphere. It was found that a transient viscosity (Kelvin element) of 10^{18} Pa s and a steady state viscosity (Maxwell element) of $>5 \times 10^{19}$ Pa s (red lines of Figure 6) can explain the satellite gravity observations within the data noise. A lower Maxwell viscosity ($<5 \times 10^{19}$ Pa s) leads to a gravity change increasing too fast and to a deviation between model and data in the case of M_{rr} (see supporting Figure S4 in Supporting Information S1). This is another interesting difference that we have not seen from previous studies of shallow events. For most shallow thrust events, a Maxwell viscosity of less than 10^{19} Pa s is favored to explain the satellite gravity observations (e.g., Broerse et al., 2015; Han et al., 2014; Panet et al., 2010). Our viscoelastic model has one uniform layer of the asthenosphere from 60 to 220 km in depth and the viscosity is constant within that layer. The viscosity of the upper mantle beneath the asthenosphere was

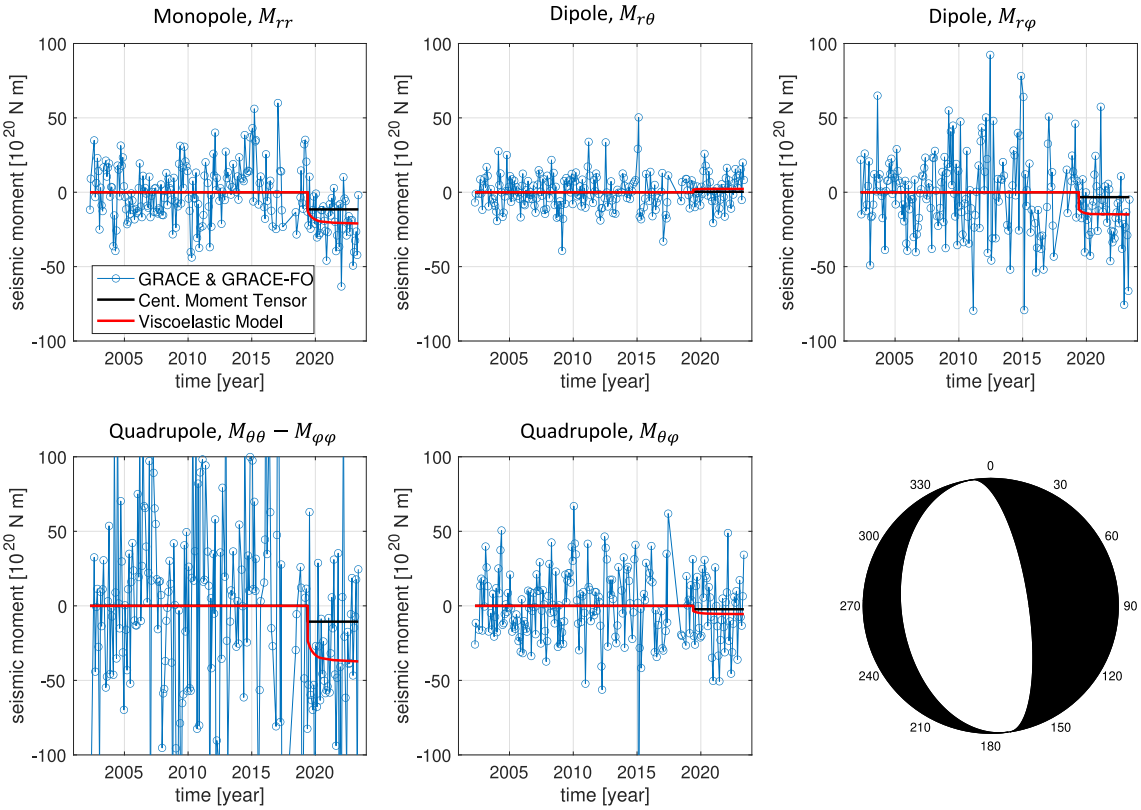

Figure 7. The same as Figure 6 but for the 2019 normal faulting earthquake in Peru.

held fixed at 5×10^{20} Pa s. The GRACE observations imply that the viscoelastic relaxation triggered by a source at intermediate depths is more effectively weighted toward a higher viscosity, closer to an upper mantle value, than that of a shallow event.

One of the best fit cases of the (elastic and viscoelastic) gravity modeling illustrates estimates of the effective moment tensor components of the 2016/17 earthquakes as shown in the last panel of Figure 6. They are 25, 2.8, −6.3, 0.7, and 1.3×10^{20} N-m for M_{rr}, $M_{r\theta}$, $M_{r\varphi}$, ($M_{\theta\theta}$−$M_{\varphi\varphi}$), and $M_{\theta\varphi}$, respectively. Except for M_{rr}, these GRACE estimates are not significantly above the noise level of each time series. In comparison, the USGS centroid moment tensor (CMT) solutions are 18, −0.8, −0.8, −2.8, and 8.9×10^{20} N-m, respectively, for the five components (see also black lines of Figure 6). If we consider viscoelastic relaxation as the only mechanism following the main events, it is primarily the low transient viscosity that is responsible for the M_{rr} gravity increase of more than a factor of 2 (from 25 or 18×10^{20} N-m to 50×10^{20} N-m), resulting in a gravity change as seen from the GRACE data 2 to 3 times larger than in the finite fault model calculation (Figure 1 *vs*. Figure 4a).

An identical analysis was conducted for the 2019 normal faulting event under Peru at 120 km depth. Figure 7 presents the gravity change observations corresponding to the five moment tensor components at the epicenter of the 2019 earthquake. The global CMT solution implies that the moment release was approximately -11×10^{20} N-m for M_{rr} and ($M_{\theta\theta}$−$M_{\varphi\varphi}$), and less than a few times 10^{20} N-m for all other components (black lines of Figure 7). With 4 years of postseismic observations, the observed gravity changes are significant only for the M_{rr} component; the noisier ($M_{\theta\theta}$−$M_{\varphi\varphi}$) measurements may become useful with additional years of data. Based on the M_{rr} observations alone, the same viscoelastic model of 10^{18} Pa s and 5×10^{19} Pa s, for the Kelvin and Maxwell viscosity, respectively, accounts for the measurements (the same model as for the 2016/2017 events), and the other model with 10^{19} Pa s for the Maxwell viscosity is also equally acceptable and indistinguishable from the case of higher viscosity (see supporting Figure S5 in Supporting Information S1). As a result of normal faulting, an extensional stress is imposed in the asthenosphere, which drives subsidence and a negative gravity change (see also Figures 3 and 5 of Han et al. (2019)). Like the case of the 2016/17 and the synthetic example in Figure 5, the

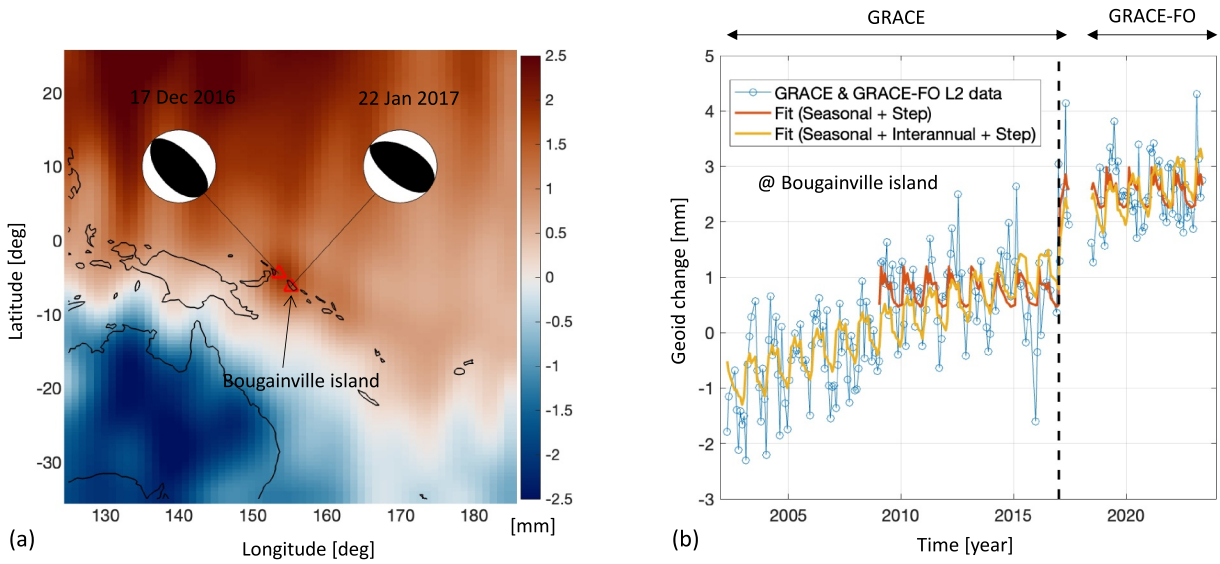

Figure 8. Similar to Figure 1, but in terms of geoid anomaly that reflects mass change over a broader region than gravity anomaly. The map in (a) shows also large positive and negative geoid changes in the Pacific, north of Papua New Guinea, and in the Australian continent, respectively. They are actually the ocean and land mass changes not associated with the 2016/2017 earthquakes (See their time series in Figure S6 in Supporting Information S1). The geoid time series at the Bougainville island (6°S, 155°E) present the step-like change after the events as well as other seasonal and inter-annual changes. Depending on the model used to fit the time-series, the step is determined to be 1.8 ± 0.1 mm (without a linear trend) and 0.7 ± 0.2 mm (with a linear trend).

postseismic change is additive to the coseismic change, which is the opposite to the observation from shallow events with higher compressibility (see Figure 2 of Han et al. (2014)).

6. Implications for Vertical Land Motion and Relative Sea Level Rise

As we discussed, the vertical land motion (VLM) is the main driver behind the observed gravity change after the 2016/2017 events east of Papua New Guinea. When aseismic slip and/or rapid viscoelastic deformation were included as suggested by the GRACE observations, the total VLM is likely to be 2–3 times larger than VLM predicted by the seismic-only models (supporting Figures S1 and S2 in Supporting Information S1). Relative sea level change (i.e., apparent change in sea level at the coast) is affected by earthquakes through VLM as well as geopotential changes. Coastal uplift reduces relative sea level, while subsidence increases relative sea level. Similarly, earthquake-induced changes in the geoidal surface (which represents the mean sea level), corresponding to the positive gravitational potential change around the epicentral region, lead to equal contributions to relative sea level change (Broerse et al., 2011). The earthquake-induced sea level changes are superimposed on the on-going sea level rise of ∼3 mm/yr in global average with some regional variations (e.g., Cazenave & Moreira, 2022; Nerem et al., 2018).

We computed the geoid change using the GRACE geopotential observations and found a localized increase over the epicentral region of the 2016/2017 earthquakes with the spatial resolution of 450 km (Figure 8a). In addition, there are other larger-scale anomalies in the Pacific, north of Papua New Guinea, and in the Australian continent. However, these are not earthquake-related, but the difference between the data before and after the earthquakes captured the interannual geoid change as well (see the time series of the Pacific and Australian anomalies in supporting Figure S6 in Supporting Information S1). The monthly time series of the geoid anomalies at Bougainville Island (6°S, 155°E) show a more complex nature to the signals than those of gravity anomalies, as geoid change reflects mass change over a broader area (Figure 8b). The geoid time series feature the seasonal, interannual and episodic (earthquake-related) changes. We determined the earthquake-induced geoid changes by considering two models that can represent the observed geoid anomaly time series: (a) the seasonal variation and Heaviside step at the mean time of the events, for the period January 2009 and May 2023 (red curve of Figure 8b) and (b) the seasonal, interannual and Heaviside step for the entire time series (yellow curve of Figure 8b). The step change estimates are 1.8 ± 0.1 mm and 0.7 ± 0.2 mm for the two cases, respectively.

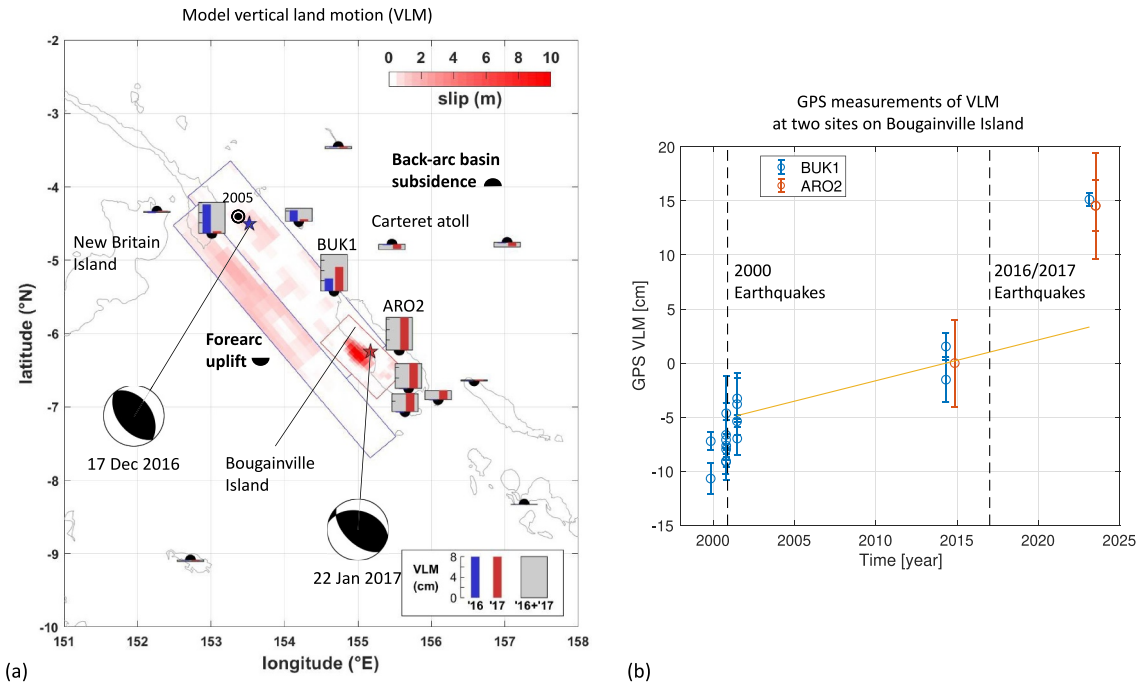

Figure 9. (a) The vertical land motion (VLM) predicted from the finite fault models available from USGS, for the 2016 and 2017 earthquakes. The vertical bars at some representative locations (including the town of Buka in the forearc and Carteret Atolls in the back-arc basin) indicate VLM from each event of 2016 (blue color) and 2017 (red color). They are computed for the coseismic case (elastic deformation) only. Additional VLM by viscoelastic relaxation and/or afterslip is predicted according to the GRACE and GRACE-FO gravity measurements. There are two campaign GPS stations, BUK1 (Buka airport) and ARO2 (Aropa airport), where the model predicts 7.1 and 6.4 cm uplift, respectively. The small bull's eye symbol is the epicenter of the earthquake of 09 September 2005 identified as the only slow outlier in Saloor and Okal's (2018) data set. (b) GPS measurements of VLM from BUK1 and ARO2 present uplift of 12–15 cm by the 2016/2017 earthquakes, depending on possible pre-existing postseismic VLM (a yellow line) after the November 2000 earthquakes occurred near the New Britain Island. The GPS measured VLM is 2–3 times larger than the predicted elastic deformation model.

The GRACE-observed geoid change was compared with the synthetic geoid change from the seismic finite fault model at the same spatial resolution of 450 km (supporting Figure S7a in Supporting Information S1) and the higher resolution of 55 km (supporting Figure S7b in Supporting Information S1). At the same spatial scale, the model predicts only 30%–50% of what GRACE observed (0.7–1.8 mm) at Bougainville Island, depending on the time-series models we introduced. This is consistent with the model gravity anomaly being two to three times smaller than the observations (Figures 1 and 4), which we attributed to large postseismic deformation. At the spatial resolution relevant to the local sea level change (supporting Figure S7b in Supporting Information S1), the model geoid change is less than 1.2 mm around Bougainville Island. The absolute sea level rise (i.e., geoid change) could be as much as 3–4 mm if the postseismic change is included.

At the same time, the models suggest that the entire Bougainville Island uplifted as a part of forearc uplift during the 2016/2017 thrust earthquakes (Figure 9a). The elastic models predict 7.1 cm uplift at Buka airport (denoted as BUK1), and 6.4 cm at Aropa airport (denoted as ARO2). Fortunately, we were able to obtain the historical GPS records from these two airport stations. The local surveyors re-occupied them recently in year 2023 and the daily mean positions were obtained and analyzed with the historical records (Figure 9b). The east and northward deformation by the 2016/2017 events were difficult to determine from these campaign GPS data sets due to the complex (micro-) plate tectonics in the region compared to available observations (Zhao et al., 2023). However, the vertical deformation from GPS data featured substantial uplift of 15 cm consistent with observations at both BUK1 and ARO2 between 2014 and 2023 (Figure 9b). The BUK1 station also has GPS records available for November 1999, October 2000, and June 2001. A sequence of Mw 8.0 strike-slip earthquake and *Mw* 7.8 thrust events (all shallow events) occurred at New Britain, Papua New Guinea (Figure 9a), in November 2000, and these events would lead to coseismic and postseismic deformation. We estimated a linear trend between year 2001 (after this earthquake sequence) and 2014 and extended the trend to year 2023 (a yellow line in Figure 9b). This linear trend serves as an upper bound to pre-existing (if any) postseismic deformation after the 2000 events as

postseismic deformation tends to decay over time and will thus be smaller than a linear change. With respect to the extrapolated linear trend, there is a remaining 12 cm of uplift in the GPS measurements in 2023. We thus conclude that the vertical deformation possibly caused at BUK1 and ARO2 by the 2016/2017 events would range between 12 cm (a lower bound assuming the maximum ongoing rebound caused by the 2000 sequence) and 15 cm (an upper bound assuming no such rebound). Such GPS-derived estimates of VLM are twice as large as predicted by the seismic model.

The geodetic (satellite gravity and ground GPS) measurements consistently estimate more than two times larger deformation than what the seismic models predict, suggesting additional deformation by aseismic slip and/or viscoelastic relaxation. The Bougainville Island region experienced significant uplift of as much as 12–15 cm since early 2017, providing a reprieve from the consequences of sea level rise. Although there is an absolute sea level rise of 3–4 mm predicted from the positive geoidal surface change, the uplift is 30–50 times larger, which essentially leads to relative sea level drop around Bougainville Island. This is opposite to the case of Samoa and American Samoa whose residents have been observing substantial subsidence of their land since the 2009 great earthquake doublet (Han et al., 2019; Huang et al., 2022). As typically seen from intermediate-depth earthquakes affecting larger areas over a shorter time interval, the "fortunate" events in 2016/2017 did not cause major damage, but they lifted the ground upwards at this critical moment of rising sea level. Using a global average (absolute) sea level rise of 3 mm/yr, each decimeter of uplift can be viewed as a reprieve of 33 years for the islanders, for example, on Bougainville Island.

However, the implications for relative sea level due to these events are variable. In particular, the earthquake-induced VLM effects are remarkably different for the low-lying Carteret Atoll, about 85 km north of Bougainville Island, located at the back-arc basin. This distance is sufficient to possibly move the atoll into a zone of subsidence in the wake of the 2016/2017 events, considering uncertainties in the finite fault and Earth models. If the ratio of postseismic to coseismic subsidence in Carteret is equal to what we infer for Bougainville Island based on GRACE and GPS data, Carteret Atoll subsided as much as a few cm in the aftermath of the earthquakes. Earthquake-induced sea level changes may thus add to existing contributions to flooding and erosion, such as El Niño Southern Oscillation-related weather extremes, anthropogenic actions and, in the long run, climate change-related sea level changes (e.g., Connell, 2018).

7. Discussion

The GRACE satellite observations recorded gravity changes approximately 2–3 times larger than what the seismic models predict for the elastic deformation alone. Since we noted that a different bulk modulus at the source may alter even the sign of the change in surface gravity, we have considered a modulus up to 10% larger than the PREM average, which corresponds to the maximum P−wave anomaly documented in subducting slabs from seismic tomography (e.g., Fukao & Obayashi, 2013), and recalculated the gravity change. The effect in surface gravity anomaly of that 10% increase in bulk modulus within the asthenosphere was found to be insignificant. As a next plausible explanation of the difference between the model and the GRACE data, we examined the viscoelastic relaxation. A bi-viscous model with Kelvin viscosity as low as 10^{18} Pa s (for the asthenosphere) was needed to model the rapid increase of gravity change right after the events (both 2016/17 and 2019), and a much weaker change afterward was reproduced with a Maxwell viscosity of $>5 \times 10^{19}$ Pa s for the 2016/17 and $>10^{19}$ Pa s for the 2019. Such short-term transient deformation was also observed after the 2018 deep Fiji earthquake and attributed to rapid viscoelastic relaxation with a low viscosity (10^{17}–10^{18} Pa s) layer near the bottom of the upper mantle (Park et al., 2023).

A peculiar rupture characteristic was also recorded from the 2016 event. Figure 10 shows radiated seismic energy versus seismic moment (Saloor & Okal, 2018) for a large worldwide data set of intermediate-depth events (80–135 km). It essentially contrasts the energy (E^E) estimated from P waves at high frequencies (0.5–10 s) and the moment (M_0) measured at much longer periods (50–200 s). Their ratio is expressed by a "slowness" parameter $\Theta = log(E^E/M_0)$, introduced by Newman and Okal (1998). This ratio is found to be more or less constant, being $\Theta = -4.9$ for shallow events, a little less (in absolute value) for intermediate and deep shocks. Shallow earthquakes can feature anomalously slow earthquakes, whose spectrum is red-shifted toward low frequencies, among them the so-called "tsunami earthquakes" whose tsunamis are bigger than expected from their conventional magnitudes (e.g., 1992 Nicaragua earthquake); their Θ can be between -5.8 and -6.5. By contrast, some "snappy" earthquakes have a blue-shifted source spectrum and result in exceptional accelerations, and hence

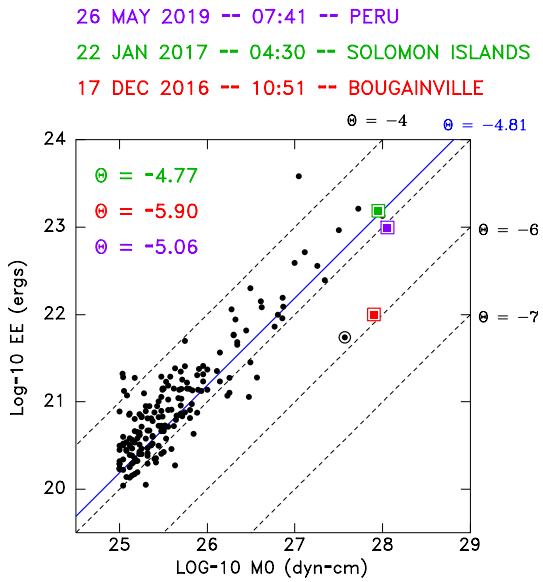

Figure 10. Energy *vs*. Moment plot and parameter Θ for intermediate-depth earthquakes including the two events of 17 December 2016 (in red) and 22 January 2017 (in green). The figure is adapted from Saloor and Okal (2018). The background black dots are their data set, with the blue line showing the average value Θ = −4.81 for the intermediate-depth bin (70−135 km). Note the clear deficiency in Θ of the 2016 event; by contrast, the 2017 event shows no anomaly. The bull's eye symbol is the outlier identified by Saloor and Okal (2018), in the general vicinity of the 2016 event, and with a seemingly anomalous Θ = −5.92. In addition, the purple symbol and labels relate to the 2019 Peruvian earthquake, for which no anomaly in Θ is noted.

destruction. Saloor and Okal (2018) found that intermediate and especially deep earthquakes are much more linearly dependent in terms of their distribution of Θ, with only one clear outlier in their entire data set of close to 600 intermediate and deep earthquakes. Their conclusions are fully upheld in a recent update of their data set, now consisting of 917 intermediate and deep earthquakes up to and including March 2023 (Okal & Saloor, 2023).

We have processed the 2016 and 2017 events using the algorithm by Saloor and Okal (2018), and found that the 2017 earthquake is typical for its depth (Θ = −4.77, the average in that depth bin being −4.81). However, the 2016 thrust event was significantly deficient, with Θ = −5.90 as opposed to −4.81 (see Figure 10), a result remarkably similar to Saloor and Okal's (2018) lone outlier (Θ = −5.92 on 09 September 2005), the hypocenters of the 2005 and 2016 events being less than 90 km apart. On the other hand, the 2019 Peru earthquake features Θ = −5.06, a value only marginally smaller than the average (−4.81), and within the scatter observed for that depth bin. We conclude that the 2019 Peruvian event does not share the anomalous character of the 2005 and 2016 earthquakes; the exceptional recurrence of those two events suggests that their source area is the subject of anomalous local processes in that section of the Solomon Islands slab, which deserve further analysis beyond the scope of the present study.

The question of the possible origin of intermediate-depth earthquakes remains wide-open. One possible model would consider oceanic plates carrying an abundance of water undergoing pressure-induced dehydration at depths typical of intermediate seismicity, the released water then functioning as a lubricant (or changing pore pressure), thus facilitating fault slip through dehydration embrittlement (e.g., Hacker et al., 2003; Houston, 2007). Another competing theory invokes a thermal runaway process in which, under enhanced pressure and temperature, rocks become malleable, facilitating slippage along faults, with localized heat generated by friction able to provide positive feedback, in turn allowing more fault slip (e.g., Kelemen & Hirth, 2007; John et al., 2009; Prieto et al., 2013). Such unusually high dissipative energy (both fractural and frictional) may promote low-frequency slip below the seismic frequency band that amplifies the largely incompressible deformation, thus contributing to enhanced surface gravity change and vertical land motion but remaining largely hidden at seismic frequencies. Only under exceptional circumstances (i.e., in the 2005 and 2016 Eastern PNG earthquakes), would this otherwise aseismic slip leak into the seismic spectrum, causing it to be red-shifted as detected in the energy-to-moment parameters Θ of these two remarkable events. While this scenario would generally reconcile the seismic, GPS and satellite gravity observations, there remains the question of the origin of the exceptional source properties of the seismogenic zone at the corner of the New Britain and Bougainville−Solomon arcs, which can only be speculated at this point.

8. Conclusions

The 2016/17 and 2019 earthquakes occurred at intermediate depths (100–150 km depth) and featured gravity changes distinct from those associated with recent large shallow, lithospheric earthquakes (<60 km depth). Modeling of the GRACE and GRACE-FO satellite measurements at a scale of 450 km indicates that deformation at depth occurred without significant volumetric change, in contrast to the deformation pattern resulting from shallow earthquakes. The satellite gravity observations demonstrated how the solid Earth responds differently to a given internal dislocation, due to different material properties at depth. The bulk modulus is 2–3 times higher at depths of 60–200 km than at crustal depths and thus inhibits expansion and contraction of the ambient rocks, leading to largely incompressible uplift during the 2016/17 thrust events, and to subsidence during the 2019 normal-faulting earthquake. Due to the absence of significant density-change effects on coseismic vertical deformation and gravity changes, the effect of postseismic viscoelastic relaxation is additive compared to the coseismic change, which is not the case for shallow earthquakes. All of these make intermediate depth earthquakes relatively easy to detect in the gravity field solutions of the GRACE and GRACE-FO satellite missions.

For the two 2016/2017 east of Papua New Guinea earthquakes and the 2019 Peru earthquake, we found GRACE gravity changes that are 2–3 higher than what we predict on basis of the seismological models. We attribute this to rapid viscoelastic relaxation or aseismic slip. For the Papua New Guinea events, GPS records of vertical displacements at Bougainville Island support this notion of additional missing (postseismic) deformation compared to the seismological models. After the 2016/2017 earthquakes, coseismic and postseismic deformation contributes to relative sea level drop at the decimeter level at Bougainville Island, and likely to relative sea level increase of a few cm at Carteret Atoll.

Data Availability Statement

The GRACE and GRACE-FO Level-2 data and additional data sets in Technical Notes 11 and 14, used in this study are publicly available through https://podaac.jpl.nasa.gov/cloud-datasets. Interested readers can start by searching GRACE-FO under Projects and Level-2 under Processing Levels. The raw GPS measurements (aka RINEX files) and position solutions as well as the analysis and plotting script are available from Han and Stanaway (2023).

Acknowledgments
We thank DLR for providing the GRACE telemetry data and JPL and CSR for producing the high-quality Level 1B and Level 2 products. We thank USGS internal reviewer Walter Mooney for his comments on an early draft, originally submitted on 9 February 2023. This work was funded by NASA's GRACE and GRACE Follow-On science team project, NASA's Earth Surface and Interior program, and Australian Research Council Discovery Program (DP170100224). Taco Broerse is funded by the Netherlands Organization for Scientific Research GO Grant ENW. GO.001.005. We thank Mr. Calvin Nalei for GPS data collection at Buka and Aropa airports. Marianne Okal at UNAVCO helped us to get GPS data from the Papua New Guinea survey team. Open access publishing facilitated by The University of Newcastle, as part of the Wiley - The University of Newcastle agreement via the Council of Australian University Librarians.

References

Ballu, V., Bouin, M. N., Siméoni, P., Crawford, W. C., Calmant, S., Boré, J. M., et al. (2011). Comparing the role of absolute sea-level rise and vertical tectonic motions in coastal flooding, Torres Island (Vanuatu). *Proceedings of the National Academy of Sciences of the United States of America*, *108*(32), 13019–13022. https://doi.org/10.1073/pnas.1102842108

Beavan, J., Wang, X., Holden, C., Wilson, K., Power, W., Prasetya, G., et al. (2010). Near-simultaneous great earthquakes at Tongan megathrust and outer rise in September 2009. *Nature*, *466*(7309), 959–963. https://doi.org/10.1038/nature09292

Becker, M., Meyssignac, B., Letetrel, C., Llovel, W., Cazenave, A., & Delcroix, T. (2012). Sea level variations at tropical Pacific islands since 1950. *Global and Planetary Change*, *80–81*, 85–98. https://doi.org/10.1016/j.gloplacha.2011.09.004

Broerse, D. B. T., Riva, R., Simons, W., Govers, R., & Vermeersen, B. (2015). Postseismic GRACE and GPS observations indicate a rheology contrast above and below the Sumatra slab. *Journal of Geophysical Research: Solid Earth*, *120*(7), 5343–5361. https://doi.org/10.1002/2015JB011951

Broerse, D. B. T., Vermeersen, L. L. A., Riva, R. E., & van der Wal, W. (2011). Ocean contribution to co-seismic crustal deformation and geoid anomalies: Application to the 2004 December 26 Sumatra–Andaman earthquake. *Earth and Planetary Science Letters*, *305*(3–4), 341–349. https://doi.org/10.1016/j.epsl.2011.03.011

Cambiotti, G., Bordoni, A., Sabadini, R., & Colli, L. (2011). GRACE gravity data help constraining seismic models of the 2004 Sumatran earthquake. *Journal of Geophysical Research*, *116*(B10), B10403. https://doi.org/10.1029/2010JB007848

Cazenave, A., & Moreira, L. (2022). Contemporary sea-level changes from global to local scales: A review. *Proceedings of the Royal Society A: Mathematical, Physical and Engineering Sciences*, *478*(2261), 20220049. https://doi.org/10.1098/rspa.2022.0049

Chao, B., & Liau, J. (2019). Gravity changes due to large earthquakes detected in grace satellite data via empirical orthogonal function analysis. *Journal of Geophysical Research: Solid Earth*, *124*(3), 3024–3035. https://doi.org/10.1029/2018JB016862

Cheng, M., & Ries, J. (2023). C20 and C30 variations from SLR for GRACE/GRACE-FO science applications. *Journal of Geophysical Research: Solid Earth*, *128*(2), e2022JB025459. https://doi.org/10.1029/2022JB025459

Connell, J. (2018). Nothing there atoll? "Farewell to the Carteret Islands". In T. Crook, & P. Rudiak-Gould (Ed.), *Pacific climate cultures: Living climate change in Oceania*. De Gruyter. https://doi.org/10.2478/9783110591415-fm

Delescluse, M., Chamot-Rooke, N., Cattin, R., Fleitout, L., Trubienko, O., & Vigny, C. (2012). April 2012 intra-oceanic seismicity off Sumatra boosted by the Banda-Aceh megathrust. *Nature*, *490*(7419), 240–244. https://doi.org/10.1038/nature11520

de Linage, C., Rivera, L., Hinderer, J., Boy, J. P., Rogister, Y., Lambotte, S., & Biancale, R. (2009). Separation of coseismic and postseismic gravity changes for the 2004 Sumatra–Andaman earthquake from 4.6 yr of GRACE observations and modelling of the coseismic change by normal-modes summation. *Geophysical Journal International*, *176*(3), 695–714. https://doi.org/10.1111/j.1365-246x.2008.04025.x

Ditmar, P. (2018). Conversion of time-varying Stokes coefficients into mass anomalies at the Earth's surface considering the Earth's oblateness. *Journal of Geodynamics*, *92*(12), 1401–1412. https://doi.org/10.1007/s00190-018-1128-0

Dziewonski, A. M., & Anderson, D. L. (1981). Preliminary reference Earth model. *Journal of Geophysical Research*, *25*(4), 297–356. https://doi.org/10.1016/0031-9201(81)90046-7

Fukao, Y., & Obayashi, M. (2013). Subducted slabs stagnant above, penetrating through, and trapped below the 660 km discontinuity. *Journal of Geophysical Research: Solid Earth*, *118*(11), 5920–5938. https://doi.org/10.1002/2013JB010466

Hacker, B. R., Peacock, S. M., Abers, G. A., & Holloway, S. D. (2003). Subduction factory 2. Are intermediate-depth earthquakes in subducting slabs linked to metamorphic dehydration reactions? *Journal of Geophysical Research*, *108*(B1), 2030. https://doi.org/10.1029/2001JB001129

Han, S.-C., Riva, R., Sauber, J., & Okal, E. (2013). Source parameter inversion for recent great earthquakes from a decade-long observation of global gravity fields. *Journal of Geophysical Research: Solid Earth*, *118*(3), 1240–1267. https://doi.org/10.1002/jgrb.50116

Han, S.-C., Sauber, J., & Pollitz, F. (2014). Broadscale postseismic gravity change following the 2011 Tohoku-Oki earthquake and implication for deformation by viscoelastic relaxation and afterslip. *Geophysical Research Letters*, *41*(16), 5797–5805. https://doi.org/10.1002/2014GL060905

Han, S.-C., Sauber, J., & Pollitz, F. (2015). Coseismic compression/dilatation and viscoelastic uplift/subsidence following the 2012 Indian Ocean earthquakes quantified from satellite gravity observations. *Geophysical Research Letters*, *42*(10), 3764–3772. https://doi.org/10.1002/2015GL063819

Han, S.-C., Sauber, J., & Pollitz, F. (2016). Postseismic gravity change after the 2006–2007 great earthquake doublet and constraints on the asthenosphere structure in the central Kuril Islands. *Geophysical Research Letters*, *43*(7), 3169–3177. https://doi.org/10.1002/2016GL068167

Han, S.-C., Sauber, J., Pollitz, F., & Ray, R. (2019). Sea level rise in the Samoan Islands escalated by viscoelastic relaxation after the 2009 Samoa-Tonga earthquake. *Journal of Geophysical Research: Solid Earth*, *124*(4), 4142–4156. https://doi.org/10.1029/2018JB017110

Han, S.-C., Shum, C. K., Bevis, M., Ji, C., & Kuo, C.-Y. (2006). Crustal dilatation observed by GRACE after the 2004 Sumatra-Andaman earthquake. *Science*, *313*(5787), 658–662. https://doi.org/10.1126/science.1128661

Han, S.-C., & Stanaway, R. (2023). GPS RINEX data and position solutions (BUK1 and ARO2) [Dataset]. Zenodo. https://doi.org/10.5281/zenodo.10164927

Heki, K., & Matsuo, K. (2010). Coseismic gravity changes of the 2010 earthquake in central Chile from satellite gravimetry. *Geophysical Research Letters*, *37*(24), L24306. https://doi.org/10.1029/2010GL045335

Houston, H. (2007). Deep earthquakes. In G. Schubert (Ed.), *Treatise on geophysics, vol. 4: Deep earthquakes, vol. 11* (pp. 321–350). Elsevier.

Huang, S. A., Sauber, J., & Ray, R. (2022). Mapping vertical land motion in challenging terrain: Six-year trends on Tutuila Island, American Samoa, with PS-InSAR, GPS, tide gauge, and satellite altimetry data. *Geophysical Research Letters*, *49*(23), e2022GL101363. https://doi.org/10.1029/2022GL101363

John, T., Medvedev, S., Rüpke, L. H., Andersen, T. B., Podladchikov, Y. Y., & Austrheim, H. (2009). Generation of intermediate-depth earthquakes by self-localizing thermal runaway. *Nature Geoscience*, *2*(2), 137–140. https://doi.org/10.1038/ngeo419

Kanamori, H., & Cipar, J. J. (1974). Focal process of the great Chilean earthquake, May 22, 1960. *Physics of the Earth and Planetary Interiors*, *9*(2), 128–136. https://doi.org/10.1016/0031-9201(74)90029-6

Kelemen, P. B., & Hirth, G. (2007). A periodic shear-heating mechanism for intermediate-depth earthquakes in the mantle. *Nature*, *446*(7137), 787–790. https://doi.org/10.1038/nature05717

Lay, T. (2015). The surge of great earthquakes from 2004 to 2014. *Earth and Planetary Science Letters*, *409*, 133–146. https://doi.org/10.1016/j.epsl.2014.10.047

Liu, W., & Yao, H. (2020). Rupture process of the 26 May 2019 Mw 8.0 northern Peru intermediate-depth earthquake and insights into its mechanism. *Geophysical Research Letters*, *47*(4), e2020GL087167. https://doi.org/10.1029/2020GL087167

Loomis, B. D., Rachlin, K. E., Wiese, D. N., Landerer, F. W., & Luthcke, S. B. (2020). Replacing GRACE/GRACE-FO C30 with satellite laser ranging: Impacts on Antarctic ice sheet mass change. *Geophysical Research Letters*, *47*(3), e2019GL085488. https://doi.org/10.1029/2019GL085488

Nerem, R. S., Beckley, B. D., Fasullo, J. T., Hamlington, B. D., Masters, D., & Mitchum, G. T. (2018). Climate-change–driven accelerated sea-level rise detected in the altimeter era. *Proceedings of the National Academy of Sciences of the United States of America*, *115*(9), 2022–2025. https://doi.org/10.1073/pnas.1717312115

Newman, A. V., & Okal, E. A. (1998). Teleseismic estimates of radiated seismic energy: The E/M0 discriminant for tsunami earthquakes. *Journal of Geophysical Research*, *103*(B11), 26885–26898. https://doi.org/10.1029/98jb02236

Ogawa, R., & Heki, K. (2007). Slow postseismic recovery of geoid depression formed by the 2004 Sumatra-Andaman Earthquake by mantle water diffusion. *Geophysical Research Letters*, *34*(6), L06313. https://doi.org/10.1029/2007GL029340

Okal, E. A., & Saloor, N. (2023). *Energy-to-moment parameter Θ for intermediate and deep earthquakes*. The International Seismological Centre Data Depository. https://doi.org/10.31905/NC8ODOAJ

Okubo, S. (1992). Gravity and potential changes due to shear and tensile faults in a half-space. *Journal of Geophysical Research*, *97*(B5), 7137–7144. https://doi.org/10.1029/92jb00178

Panet, I., Mikhailov, V., Diament, M., Pollitz, F., King, G., de Viron, O., et al. (2007). Coseismic and post-seismic signatures of the Sumatra 2004 December and 2005 March earthquakes in GRACE satellite gravity. *Geophysical Journal International*, *171*(1), 177–190. https://doi.org/10.1111/j.1365-246X.2007.03525.x

Panet, I., Pollitz, F., Mikhailov, V., Diament, M., Banerjee, P., & Grijalva, K. (2010). Upper mantle rheology from GRACE and GPS postseismic deformation after the 2004 Sumatra-Andaman earthquake. *Geochemistry, Geophysics, Geosystems*, *11*(6), Q06008. https://doi.org/10.1029/2009GC002905

Park, S., Avouac, J. P., Zhan, Z., & Gualandi, A. (2023). Weak upper-mantle base revealed by postseismic deformation of a deep earthquake. *Nature*, *615*(7952), 455–460. https://doi.org/10.1038/s41586-022-05689-8

Pollitz, F. (1997a). Gravity anomaly from faulting on a layered spherical Earth with application to central Japan. *Physics of the Earth and Planetary Interiors*, *99*(3–4), 259–271. https://doi.org/10.1016/s0031-9201(96)03204-9

Pollitz, F. F. (1992). Postseismic relaxation theory on the spherical Earth. *Bulletin of the Seismological Society of America*, *82*, 422–453.

Pollitz, F. F. (1996). Coseismic deformation from earthquake faulting on a layered spherical Earth. *Geophysical Journal International*, *125*(1), 1–14. https://doi.org/10.1111/j.1365-246X.1996.tb06530.x

Pollitz, F. F. (1997b). Gravitational-viscoelastic postseismic relaxation on a layered spherical Earth. *Journal of Geophysical Research*, *102*(B8), 17921–17941. https://doi.org/10.1029/97JB01277

Prieto, G. A., Florez, M., Barrett, S. A., Beroza, G. C., Pedraza, P., Blanco, J. F., & Poveda, E. (2013). Seismic evidence for thermal runaway during intermediate-depth earthquake rupture. *Geophysical Research Letters*, *40*(23), 6064–6068. https://doi.org/10.1002/2013GL058109

Rodell, M. (2014). Satellite-based estimates of groundwater depletion. In *A paper presented at international workshop on going beyond agri-cultural water productivity*. World Bank.

Saloor, N., & Okal, E. A. (2018). Extension of the energy-to-moment parameter Θ to intermediate and deep earthquakes. *Physics of the Earth and Planetary Interiors*, *274*, 37–48. https://doi.org/10.1016/j.pepi.2017.10.006

Savage, J. C. (1983). A dislocation model of strain accumulation and release at a subduction zone. *Journal of Geophysical Research*, *88*(B6), 4984–4996. https://doi.org/10.1029/jb088ib06p04984

Sun, W. K., & Okubo, S. H. (1993). Surface-potential and gravity changes due to internal dislocations in a spherical Earth: 1. Theory for a point dislocation. *Geophysical Journal International*, *114*(3), 569–592. https://doi.org/10.1111/j.1365-246x.1993.tb06988.x

Tamisiea, M. E., Mitrovica, J. X., & Davis, J. L. (2007). GRACE gravity data constrain ancient ice geometries and continental dynamics over Laurentia. *Science*, *316*(5826), 881–883. https://doi.org/10.1126/science.1137157

Tanaka, Y. (2023). Coseismic gravity changes and crustal deformation induced by the 2018 Fiji deep-focus earthquake observed by GRACE and GRACE-FO satellites. *Remote Sensing*, *15*(2), 495. https://doi.org/10.3390/rs15020495

Tanaka, Y., Heki, K., Matsuo, K., & Shestakov, N. V. (2015). Crustal subsidence observed by GRACE after the 2013 Okhotsk deep-focus earthquake. *Geophysical Research Letters*, *42*(9), 3204–3209. https://doi.org/10.1002/2015gl063838

Tapley, B., Watkins, M. M., Flechtner, F., Reigber, C., Bettadpur, S., Rodell, M., et al. (2019). Contributions of GRACE to understanding climate change. *Nature Climate Change*, *9*(5), 358–369. https://doi.org/10.1038/s41558-019-0456-2

Vallée, M., Xie, Y., Grandin, R., Villegas-Lanza, J. C., Nocquet, J. M., Vaca, S., et al. (2023). Self-reactivated rupture during the 2019 $M_w = 8$ northern Peru intraslab earthquake, 601, 117886. *Earth and Planetary Science Letters*, *601*, 117886. https://doi.org/10.1016/j.epsl.2022.117886

Wahr, J., Molenaar, M., & Bryan, F. (1998). Time variability of the Earth's gravity field: Hydrological and oceanic effects and their possible detection using GRACE. *Journal of Geophysical Research*, *108*(B12), 30205–30229. https://doi.org/10.1029/98jb02844

Xu, C., Su, X., Liu, T., & Sun, W. (2017). Geodetic observations of the co- and post-seismic deformation of the 2013 Okhotsk Sea deep-focus earthquake. *Geophysical Journal International*, *209*(3), 1924–1933. https://doi.org/10.1093/gji/ggx123

Ye, L., Lay, T., & Kanamori, H. (2020). Anomalously low aftershock productivity of the 2019 Mw 8.0 energetic intermediate-depth faulting beneath Peru. *Earth and Planetary Science Letters*, *549*, 116528. https://doi.org/10.1016/j.epsl.2020.116528

Yuan, D.-N. (2019). *GRACE Follow-On JPL level-2 processing standards document for level-2 product release 06*. Jet Propulsion Laboratory. California Institute of Technology.

Zhao, S., McClusky, S., Cummins, P. R., Miller, M. S., & Nugroho, H. (2023). New insights into crustal deformation of the Indonesia–Australia–New Guinea collision zone from a broad-scale kinematic model. *Journal of Geophysical Research: Solid Earth*, *128*(2), e2022JB024810. https://doi.org/10.1029/2022JB024810